Applied and
Computational
Mathematics
Division

NISTIR 90-4283

Center for Computing and Applied Mathematics

Stabilization of Taylor-Couette Flow due to Time-Periodic Outer Cylinder Oscillation

B.T. Murray, G.B. McFadden, and S.R. Coriell

April 1990

U.S. DEPARTMENT OF COMMERCE
National Institute of Standards and Technology
Gaithersburg, MD 20899

Stabilization of Taylor-Couette Flow due to Time-Periodic Outer Cylinder Oscillation

B. T. Murray, G. B. McFadden, and S. R. Coriell
National Institute of Standards and Technology
Gaithersburg, Maryland 20899, USA

Abstract

The linear stability of circular Couette flow between concentric infinite cylinders is considered for the case when the inner cylinder is rotated at a constant angular velocity and the outer cylinder is driven sinusoidally in time with zero mean rotation. This configuration was studied experimentally by Walsh and Donnelly. The critical Reynolds numbers calculated from linear stability theory agree well with the experimental values, except at large modulation amplitudes and small frequencies. The theoretical values are obtained using Floquet theory implemented in two distinct approaches: 1) a truncated Fourier series representation in time and 2) a fundamental solution matrix based on a Chebyshev-pseudospectral representation in space. For large amplitude, low frequency modulation, the linear eigenfunctions are temporally complex, consisting of a quiescent interval followed by rapid change in the perturbed flow velocities.

1. Introduction

In 1923 G.I. Taylor considered the stability of the steady Couette flow between rotating cylinders and discovered a transition to steady axisymmetric toroidal rolls ("Taylor vortices"), obtaining agreement between the measured values of the critical rotation rates and his theoretical predictions [1]. In the last thirty years, a substantial amount of research has been conducted on various aspects of Taylor-Couette flow, including the effect of time-periodic forcing of the cylinder rotation rates. Beginning with the experimental work of Donnelly et al [2], [3], where it was observed that temporal modulation of the inner cylinder angular velocity provides stabilization, the problem has served as an important model for gaining understanding into the effects of time-periodic forcing.

The present study is an outgrowth of a research effort to understand the interaction of a solidification interface, and its associated interfacial instabilities, with some of the fundamental hydrodynamic instabilities [4]. These problems are relevant to the area of materials processing, in particular, growth of a solid from the melt. For the Taylor-Couette problem, recent studies by McFadden et al have demonstrated that a solidification interface can significantly alter the centrifugal instability for steady rotation [5], [6], and the effect of time-periodic rotation is now being addressed. In developing the linear theory for the interaction of modulated Taylor-Couette flow with a solidification interface, the isothermal problem subject to time-periodic oscillation was used to test the solution procedures. After reviewing the literature on this problem, it was found that some discrepancies remain between the existing experimental results and theoretical predictions.

Carmi and Tustaniwskyj [7] performed a comprehensive study of the linear theory onset conditions for sinusoidal torsional oscillation of the cylinders using Floquet theory. The study was comprehensive, in that several variations of forcing conditions were considered, with and without mean rotation, for a finite-gap width and for a gap width that approximates the narrow-gap limit. Their analysis predicts destabilization predominantly as a result of modulation. Donnelly and colleagues have conducted several of the more recent experimental studies on the effects of temporal modulation. For the particular case of steady rotation of the inner cylinder and sinusoidal torsional oscillation of the outer cylinder about a zero mean. Walsh and Donnelly [8] observed stabilization due to the modulation, while the linear theory of Carmi and Tustaniwskyj [7] predicts destabilization. A recent theoretical analysis by Barenghi and Jones [9] yields much better agreement between linear theory and experiment for one set of the Walsh and Donnelly experiments; however, this set of conditions was not the focus of their study, and the experimental conditions yielding the greatest stabilization were not considered.

The present study provides a more complete comparison with the cases considered experimentally by Walsh and Donnelly [8]. A thorough theoretical investigation is conducted based on linear theory employing Floquet analysis in two independent approaches to the numerical solution. A detailed description of the linear theory eigenmodes, both spatial and temporal is included. Although limited to linear behavior, the comprehensive study provides better understanding into the complex nature of the response to temporally-periodic forcing in the Taylor-Couette problem.

2. Theory

Briefly, the governing equations are the continuity equation and the incompressible Navier-Stokes equations for the velocity, $\boldsymbol{u}$, and the pressure, p,

$$\nabla \cdot \boldsymbol{u} = 0, \tag{1a}$$

$$\frac{\partial \boldsymbol{u}}{\partial t} + (\boldsymbol{u} \cdot \nabla)\boldsymbol{u} + \frac{1}{\rho}\nabla p = \nu \nabla^2 \boldsymbol{u}, \tag{1b}$$

where ρ is the density and ν is the kinematic viscosity. For cylindrical-polar coordinates (r, θ, z), the velocity components are $\boldsymbol{u} = (u, v, w)$ in the radial, azimuthal, and axial directions, respectively. The fluid occupies the annular region $R_1 < r < R_2$, where R_1 is the inner cylinder radius and R_2 is the outer cylinder radius. For the stability analysis, the cylinder is assumed to be infinite in the axial direction.

We focus the analysis on time-periodic rotation of the outer cylinder about a zero mean, while the inner cylinder rotates with a constant angular velocity Ω_1. The angular velocity of the outer cylinder is assumed to be $\Omega_2(t) = \epsilon\Omega_1 \cos \omega t$, where ω is the forcing frequency. The boundary conditions on the velocity components are the no-slip and no-penetration conditions at solid boundaries; therefore, the azimuthal velocity at the inner cylinder is $v_1 = R_1\Omega_1$ and at the outer cylinder is $v_2 = R_2\Omega_2(t)$. The remaining velocity components are zero at both boundaries.

We next choose dimensionless variables. The length scale is chosen to be the fluid gap width $d = R_2 - R_1$, the time scale is chosen to be d^2/ν, and the velocity scale is chosen to be ν/d. We retain the same notation for all variables, which will henceforth be dimensionless. The choice of scaling introduces the Reynolds number in the boundary condition, which is given by $R_e = \Omega_1 d^2/\nu$. The fluid region then occupies the range $\eta/(1-\eta) < r < 1/(1-\eta)$, where $\eta = R_1/R_2$.

3. Base State

The base state is given by $u = 0$, $v = v^{(0)}(r,t)$, and $w = 0$. The dimensionless azimuthal velocity satisfies

$$\frac{\partial v^{(0)}}{\partial t} = \left(\frac{\partial^2 v^{(0)}}{\partial r^2} + \frac{1}{r}\frac{\partial v^{(0)}}{\partial r} - \frac{v^{(0)}}{r^2} \right), \tag{2a}$$

with the boundary conditions,

$$v^{(0)}(\eta/(1-\eta), t) = \frac{\eta R_e}{1-\eta}, \tag{2b}$$

and

$$v^{(0)}(1/(1-\eta), t) = \frac{\epsilon R_e}{1-\eta} \cos \omega t. \tag{2c}$$

The solution to the above linear problem for the base flow is written as the superposition of a steady and a periodic component, $v^{(0)} = V_s(r) + V_p(r,t)$. The steady solution is found by setting the right-hand side of Eq. (2a) equal to zero, and applying the steady part of the boundary conditions. The steady component of the base flow is

$$V_s = \frac{R_e}{1-\eta^2}\left[\frac{\eta^2}{(1-\eta)^2}\frac{1}{r} - \eta^2 r\right]. \tag{3}$$

An analytic solution for the periodic component of the base flow solution can be written in terms of Kelvin functions. However, because the solution to the stability problem must be determined numerically, it is often more efficient to calculate the periodic component of the base flow numerically in the same manner used to calculate the perturbed flow.

4. Linearized equations

For the linear stability analysis of the time-dependent base state, the total flow field variables are written as the superposition of the base state component and a perturbation. The perturbed quantities are Fourier analyzed in the azimuthal and axial directions, so that we write

$$\begin{pmatrix} u(r,z,\phi,t) \\ v(r,z,\phi,t) \\ w(r,z,\phi,t) \\ p(r,z,\phi,t) \end{pmatrix} = \begin{pmatrix} 0 \\ v^{(0)}(r,t) \\ 0 \\ p^{(0)}(r,t) \end{pmatrix} + \begin{pmatrix} \hat{u}(r,t) \\ \hat{v}(r,t), \\ \hat{w}(r,t) \\ \hat{p}(r,t) \end{pmatrix} \exp(in\phi + iaz), \tag{4}$$

where a is the nondimensional axial wave number and n is the azimuthal mode number. The base state components are denoted by a zero superscript (e.g., $v^{(0)}$) and the quantities $\hat{u}$, $\hat{v}$, $\hat{w}$, $\hat{p}$ are the perturbation amplitudes. Note that only axisymmetric disturbances ($n = 0$) will be used to obtain the stability results presented here; however, the analysis is formulated for the general nonaxisymmetric case.

The governing equations for the perturbation quantities are obtained by substituting the above expansion into the dimensionless form of Eq. (1) and linearizing in the perturbation quantities:

$$D\hat{u} + \frac{\hat{u}}{r} + \frac{in\hat{v}}{r} + ia\hat{w} = 0, \tag{5a}$$

$$\frac{\partial \hat{u}}{\partial t} + in\frac{v^{(0)}}{r}\hat{u} - 2\frac{v^{(0)}}{r}\hat{v} + D\hat{p} = D^2\hat{u} + \frac{D\hat{u}}{r} - \frac{n^2\hat{u}}{r^2} - a^2\hat{u} - \frac{\hat{u}}{r^2} - \frac{2in\hat{v}}{r^2}, \tag{5b}$$

$$\frac{\partial \hat{v}}{\partial t} + in\frac{v^{(0)}}{r}\hat{v} + D_* v^{(0)}(r,t)\hat{u} + \frac{in\hat{p}}{r} = D^2\hat{v} + \frac{D\hat{v}}{r} - \frac{n^2\hat{v}}{r^2} - a^2\hat{v} - \frac{\hat{v}}{r^2} + \frac{2in\hat{u}}{r^2}, \tag{5c}$$

$$\frac{\partial \hat{w}}{\partial t} + in\frac{v^{(0)}}{r}\hat{w} + ia\hat{p} = D^2\hat{w} + \frac{D\hat{w}}{r} - \frac{n^2\hat{w}}{r^2} - a^2\hat{w}, \tag{5d}$$

for $\eta/(1-\eta) < r < 1/(1-\eta)$. Here $D = \partial/\partial r$ and $D_* = \partial/\partial r + 1/r$.

The order of the system is reduced by differentiating Eq. (5a) with respect to r and subtracting it from Eq. (5b) yielding,

$$\frac{\partial \hat{u}}{\partial t} + in\frac{v^{(0)}}{r}\hat{u} - 2\frac{v^{(0)}}{r}\hat{v} + D\hat{p} = -\frac{n^2\hat{u}}{r^2} - a^2\hat{u} - i[\frac{nD\hat{v}}{r} + \frac{n\hat{v}}{r^2} + aD\hat{w}]. \tag{6}$$

The set of equations (5a), (5c), (5d), and (6) yield a sixth-order system which is closed by the six boundary conditions $\hat{u} = \hat{v} = \hat{w} = 0$ imposed at $r = \eta/(1-\eta)$ and $r = 1/(1-\eta)$.

Alternatively, one can eliminate $\hat{w}$ and $\hat{p}$ from the set of equations by straightforward manipulation to obtain a fourth-order equation in r for the quantity $\hat{u}$ and a second-order equation for $\hat{v}$. This is a commonly-used formulation for hydrodynamic stability problems, so the equations are not given here (see Carmi and Tustaniwskyj [7] for the full nonaxisymmetric equations). The boundary conditions in this form become $\hat{v} = \hat{u} = D\hat{u} = 0$ at the inner and outer boundaries. As discussed in the next section, two different numerical approaches are used to solve the stability problem. In the first approach, the set of equations retaining all the variables shown above is used, while in the second approach, the reduced set of equations in terms of $\hat{u}$ and $\hat{v}$ alone is advantageous.

5. Numerical Treatment

The set of equations for the perturbation quantities are linear partial differential equations in one space variable and time. The equations contain time periodic coefficients, and so Floquet theory can be used to investigate the stability of the system. Two distinct implementations of Floquet theory are employed. In the first approach, the time-periodic part of the solution is represented by a truncated complex Fourier series in time. This approach was employed by Hall [10] and by Seminara and Hall [11] for similar stability problems. In this approach, a perturbation quantity $\hat{f}(r,t)$ is represented by the product of a periodic Fourier series and an exponential term with complex growth rate σ,

$$\hat{f}(r,t) = e^{\sigma t} \sum_{|m| \leq M} f_m(r) e^{im\omega t},$$

The real part of σ determines the stability of the base solution. Substitution of the series expansion into the equations and boundary conditions above yields a large set of coupled two-point boundary value problems in the spatial variable r for the Fourier coefficients, $f_m(r)$. The set of equations is complex and contains the growth rate σ as a parameter.

The set of coupled two-point boundary value problems, subject to the homogeneous boundary conditions, yields an eigenvalue problem that is solved using the computer code SUPORT in a similar manner as the one described in [12]. The SUPORT code [13] solves the set of linear coupled two-point boundary value problems using superposition of numerically integrated solutions. An orthonormalization procedure is used to assure linear independence of the intermediate solutions. The user has a choice of variable-step integration schemes. For all the results presented, a high-order Adams-type procedure was used.

The base state subject to periodic forcing is linearly stable if for all disturbances $\sigma_r < 0$, where σ_r is the real part of σ. For the condition of neutral stability ($\sigma_r = 0$), the solution of the eigenvalue problem for the full set of coupled complex Fourier modes yields the Reynolds number and the imaginary part of the growth rate (σ_i) for fixed values of the remaining parameters. Using the full set of equations for the problem posed here, σ_i is found to be either zero (synchronous response) or $\omega/2$ (subharmonic response). By fixing the value of σ_i for either synchronous or subharmonic response, symmetry relationships between the negative and positive index Fourier modes can be used to halve the number of unknowns required to solve for the Reynolds number alone. For axisymmetric disturbances, a set of $12M + 12$ ordinary differential equations for the coupled, complex temporal Fourier modes must be solved. The value of M used depends on the parameter values, in particular, the value of the forcing frequency. Lower frequency calculations are more temporally complicated and require a greater number of Fourier modes in time. For the results presented, the value of M ranged from 4 to 24, depending on frequency. A discussion of the accuracy and convergence of this approach is contained in the next section.

The periodic part of the base flow solution is obtained by assuming

$$V_p(r,t) = Real[V(r)e^{i\omega t}]$$

where the real part corresponds to cosine forcing at the boundaries. It is through the periodic time dependence of the base flow solution terms in the perturbation equations that the individual temporal Fourier solution modes are coupled. Substituting the above form into the equation and boundary conditions given by Eq. (2) yields a two-point boundary value problem for the complex amplitude function $V(r)$, which has an analytic solution in the form of Kelvin functions of the first and second kind. Because a variable stepsize is used to integrate the perturbation equations numerically, it is computationally more efficient to solve for $V(r)$ using SUPORT, rather than evaluate the Kelvin functions which comprise the analytic solution. Calculating the complex amplitude function $V(r)$ numerically in this manner does not degrade the accuracy of the required base flow solution.

The second numerical approach employed to solve the stability problem consists of approximating the spatial behavior of the solutions, using the equation set for $\hat{u}$ and $\hat{v}$ alone, via the pseudospectral technique in the physical domain, as described in references [14] and [15]. The approach corresponds to expanding the solutions in terms of truncated series of Chebyshev polynomials $T_n(s)$,

$$\hat{u}(r,t) = \sum_{n=0}^{N} u_n(t)\, T_n(s),$$

$$\hat{v}(r,t) = \sum_{n=0}^{N} v_n(t)\, T_n(s),$$

where $s = 2(r - \eta/(1-\eta)) - 1$. The pseudospectral discretization requires that the solution expansions satisfy the governing equations at specific collocation points for the Chebyshev polynomials. When implemented in the physical domain, the unknowns are the solution values at the collocation points, instead of the expansion coefficients as in purely spectral methods.

In the pseudospectral approach, the spatial differential operators in the governing partial differential equations are replaced by discrete matrix operators. As a result, the governing set of partial differential equations and boundary conditions becomes a set of coupled ordinary differential-algebraic equations in time for the unknown solution values at the collocation points. The algebraic equations result from the boundary conditions. Because the size of the set of coupled equations depends on the number of original partial differential equations, the size is minimized by using the equations formulated in terms of $\hat{u}$ and $\hat{v}$ alone, as discussed in the previous section; the total number of unknowns in this formulation is $2(N+1)$. In this numerical solution approach, the computational effort for determining the periodic component of the base flow by numerical integration or by evaluation of the Kelvin functions is equivalent, since the amplitude values $V(r)$ are required only at fixed collocation points (i.e., they need only be calculated once and stored).

The computer code DASSL [16] is used to integrate the differential-algebraic system in time. The algorithm uses backward differentiation with up to fifth-order accuracy obtained using a multi-step approach. The implicit integration procedure is appropriate for the integration of the equation set obtained from a Chebyshev spatial discretization. Also, because differential-algebraic systems often behave like systems of stiff differential equations, they require that special error estimation schemes be used in order to obtain stable, accurate solutions [17].

In this second approach, Floquet analysis is implemented by constructing a $K \times K$ fundamental solution matrix, where K is the number of differential equations ($K = 2N - 4$). The K columns of this matrix are linearly independent calculated solutions for the unknowns at the end of one forcing period. The eigenvalues of this matrix are the Floquet multipliers from which the complex growth rate σ is obtained. The advantage of the second approach is that it yields K values of σ resulting from the discrete solution modes, providing several eigenvalues that are accurate approximations to the spectrum. Since periodic forcing can excite different temporal response (i.e., subharmonic versus synchronous), knowledge of the relative stability of various modes provided by the σ values simplifies the determination of the critical stability boundaries in parameter space.

The two distinct numerical solution approaches provide an independent check on the calculated results. In addition, each of the two approaches has advantages and disadvantages depending on the nature of the solution. For example, if the spatial variation is limited more to the boundary regions of the domain, the SUPORT approach with its variable mesh increment can optimize the computation effort for a given global accuracy; while for complicated temporal behavior, the time integration scheme of the second approach may be better, since the temporal Fourier representation may converge slowly and require an impractical number of terms for reasonable accuracy.

6. Results

As discussed in the introduction, the focus of the present study is a comprehensive comparison of linear stability theory predictions for the onset conditions with the experimental results of Walsh and Donnelly [8]. Only one type of boundary forcing is considered; the case when the inner cylinder rotates at constant angular velocity and the outer cylinder is modulated about a zero mean. In the experiments, Walsh and Donnelly varied the gap width, the forcing frequency, and the outer cylinder angular velocity modulation amplitude. For this particular configuration, it was found in the experiments that the modulation stabilizes the flow when compared to the case with zero outer cylinder rotation.

For the present calculations, only axisymmetric disturbances ($n = 0$) are considered. We present the calculated results here in terms of the parameters used by Walsh and Donnelly and those used in earlier theoretical studies [7]. The Reynolds number $\tilde{R}_e$ used in the previous studies is related to the Reynolds number that appears in the theoretical formulation here by $\tilde{R}_e = R_e\sqrt{\eta/(1-\eta)}$. The dimensionless forcing frequency used previously, γ, is related to the dimensionless frequency of the present formulation by $\omega = 2\gamma^2$; the use of γ rather than ω compacts the frequency scale. The remaining parameters η and ϵ, the radius ratio and dimensionless modulation amplitude, respectively, are defined in Section 3. For simplicity in all the figures that follow, we have shifted the origin of r so that r ranges from 1 to 2 instead of $\eta/(1-\eta)$ to $1/(1-\eta)$.

In Figs. 1 and 2, the base flow as a function of r for nine different fractional times covering half a cycle is shown for two values of modulation frequency, $\gamma = 2$ and 6, respectively. The base flow velocity is normalized by the maximum velocity of the outer cylinder. For clarity only half the cycle is shown. For the higher frequency, $\gamma = 6$, the effect of the outer cylinder modulation is confined to the vicinity of the outer boundary, whereas for the lower frequency $\gamma = 2$, the effect of the modulation spans the entire domain.

In the experiments of Walsh and Donnelly, three radius ratios ($\eta = 0.719, 0.88$ and 0.95) and two modulation amplitudes ($\epsilon = 0.5$ and 1.5) were investigated for several different forcing frequencies, γ. Calculated results are presented for the same combinations of parameters as the experiments for a larger and more continuous range of frequencies. In Fig. 3, we show the critical Reynolds number $\tilde{R}_c$ (the absolute minimum of $\tilde{R}_e$ as a function of wavenumber, a) versus γ for radius ratio $\eta = 0.719$ and modulation amplitude $\epsilon = 1.5$. An ϵ value of 1.5 means that the maximum amplitude of the periodic angular velocity of the outer cylinder is 1.5 times greater than the steady angular velocity value of the inner cylinder. In the figure, the curves represent the present linear theory predictions, while the individual points are from the experiments [8]. Points below the curves are stable according to linear theory, while points lying above are unstable. As can be seen, the agreement is quite good.

For large frequencies, the predicted critical values asymptote to the value for a stationary outer cylinder, since the effects of the modulation are confined to a thin layer near the outer boundary. The calculated curve approaches the critical value for a stationary outer cylinder, which for $\eta = 0.719$ corresponds to $\tilde{R}_c = 51.04$. The theoretical predictions consist of two individual curves. The curve on the right is a synchronous mode, for which the imaginary part of the growth rate σ vanishes. The narrow parabolically shaped curve corresponds to subharmonic response, where σ_i is equal to $\omega/2$. In the experiments, there was no means for monitoring the temporal character of the instability as onset ensued, so the distinction between synchronous or subharmonic response could not be made. The maximum amount of stabilization occurs for γ in the range of 3 to 4.

In Fig. 4, we show the critical values for the case where the radius ratio $\eta = 0.88$ and $\epsilon = 0.5$. Again, the solid curve is the linear theory predictions and the individual points are from Walsh and Donnelly's experiments. The amount of stabilization obtained in this case is significantly less than the previous case, for which the maximum modulation angular velocity was 1.5 times the constant angular velocity of the inner cylinder. For the range of frequencies considered, only synchronous response is obtained at onset from the theory with this lower value of ϵ. The agreement between theory and experiment is again quite good. For $\eta = 0.88$, the critical value for the unmodulated case is $\tilde{R}_c = 44.49$, which is the asymptotic value of the theoretical results as the frequency becomes large. Barenghi and Jones [9] present a curve of $\tilde{R}_c$ versus γ based on their linear theory calculations for this set of parameters. The maximum stabilization predicted by their calculations agrees very well with our calculations. However, their calculated values of $\tilde{R}_c$ do not decrease as sharply as ours for γ greater than about 1.25.

Again for $\eta = 0.88$, Fig. 5 shows the onset conditions in the case when the modulation amplitude is increased to $\epsilon = 1.5$. The theoretical curve exhibits similar structure as the case shown in Fig. 3, with subharmonic response again being obtained. Only five experimental data points for a narrow range of frequencies were provided for this case. At lower frequencies the theoretical stability boundary consists of parabolic regions of both subharmonic and synchronous response, with the overall trend being greater and greater stabilization. For this case, the agreement between the theory and experiment is less satisfactory. Except for one point, the experimental values lie below the theoretical curve. The primary difference between this case and the one shown in Fig. 3 is the frequency range of the data.

The final comparison with the experimental data is presented in Table 1. For $\eta = 0.88$ and a fixed frequency of $\gamma = 2.3$, the modulation amplitude is increased from $\epsilon = 0.3$ to 2.0. For modulation amplitudes below 1.0, the agreement between theory and experiment is good; however, for the values $\epsilon = 1.5$ and 2.0, the theoretical predictions are considerably higher than the experimental values. Note that the temporal response obtained from the theory is synchronous for all but the largest value of ϵ.

Walsh and Donnelly also presented four data points for $\eta = 0.95$ and $\epsilon = 0.5$ with γ in the range 0.6 to 0.9. The $\tilde{R}_c$ from the experimental data is approximately 45 within the experimental error for the range of γ covered. The theory predicts $\tilde{R}_c$ of 45.8 to 45.9 over this range, which is in good agreement with the experimental data. The unmodulated $\tilde{R}_c$ is 42.4 , so only a small amount of stabilization occurs for this case.

In order to better understand the results, and perhaps explain the discrepancy for the high modulation amplitude case shown in Fig. 5, the structure of the linear eigenmodes was investigated both spatially and temporally for $\eta = 0.88$, $\epsilon = 1.5$ and for frequencies $\gamma = 2$ and 6. For the higher frequency, Fig. 6 shows three-dimensional plots of the $\hat{u}$ and $\hat{v}$ velocity components as functions of the radial coordinate, r, and time (normalized over one period). For this high-frequency, synchronous case, the spatial and temporal structure of the eigenmodes is fairly simple, having a single maximum in space and being roughly sinusoidal in time. For $\gamma = 2$, the critical Reynolds number ($\tilde{R}_c = 94.0$) corresponds to a subharmonic mode, but there is also a synchronous mode close by with $\tilde{R}_e = 95.1$. In Fig. 7, the velocity components for the synchronous mode are shown in order to compare the effect of the frequency on the solution behavior for the same type of temporal response. In contrast to the high frequency solution, at $\gamma = 2$, both the spatial and temporal behavior are complicated; the temporal behavior consists of a quiescent interval present for nearly one-half the period followed by rapid increase in the velocity amplitudes. In order to better view the structure, the solutions are plotted from $t = 0.25$ to 1.25, so that the nonzero regions appear in the interior of the plots and not at the edges.

Three-dimensional plots of the velocity components for the subharmonic mode at $\gamma = 2$ are shown in Fig. 8. Since the temporal response is subharmonic, the velocities are plotted over two periods. Similar to the synchronous mode at the lower frequency, there are quiescent intervals followed by rapid change in the amplitudes over a short period of time. In the subharmonic case, the rapid change in amplitude occurs once every forcing period, but alternates in direction (positive or negative) so that the solution is periodic over twice the forcing period. For the synchronous case, the rapid change in amplitude is always in the same direction and the period of the flow is the same as the forcing period. Here, the solutions are plotted from $t = 0.5$ to 2.5 to better show the behavior. Given the similarity of the temporal structure (except for the change in sign of the subharmonic mode), it is not surprising that the Reynolds numbers are approximately the same for both modes. However, there is a shift in the critical wavenumber between the two modes, with $a = 3.10$ for the synchronous mode and $a = 4.35$ for the subharmonic mode.

Fig. 6 indicates that for large γ, the spatial and temporal behavior is simple, whereas for small γ Figs. 7 and 8 indicate that the temporal behavior is complicated. To further illustrate this in Fig. 9, we show convergence of the temporal Fourier coefficients for the $\hat{v}$ component of velocity. The results correspond to the two cases shown in Figs. 6 and 7, representing $\gamma = 6$ and 2, respectively. For the larger γ the Fourier coefficients decay rapidly, while for the smaller γ a large number of coefficients are required to obtain an accurate solution. The difficulty in obtaining accurate solutions at low frequencies was also discussed by Barenghi and Jones [9], where they show that $\tilde{R}_c$ values below the unmodulated value can be obtained with insufficient temporal resolution. They attribute this as the reason why the calculations of Carmi and Tustaniwskyj [7] predict destabilization for the specific boundary forcing case considered here.

While the spatial structure of the eigensolutions is less complicated than the temporal structure, it is equally important to assure that proper resolution is obtained. Both of the numerical approaches employed here provide for high spatial accuracy. The SUPORT approach achieves high accuracy through the use of a variable step-size high-order Adams integrator. The Chebyshev-pseudospectral representation of the second solution approach is also highly accurate as displayed in Fig. 10 by the decay of the Chebyshev coefficients of the $\hat{v}$ velocity for the same γ values as Fig. 9. Typically, twelve or sixteen Chebyshev modes were used for the present calculations, for which the coefficients have decayed by six orders of magnitude. Clearly, Fig. 10 also indicates that the spatial complexity does not depend significantly on γ.

The variation $\tilde{R}_e$ with wavenumber, a, for $\gamma = 2$, $\eta = 0.88$, and $\epsilon = 1.5$ is shown in Fig. 11. As is apparent from this figure, the minima of the two lowest curves (synchronous and subharmonic) occur at approximately the same Reynolds number with the absolute minimum on the subharmonic curve. With a slight increase in γ, the absolute minimum occurs on the synchronous curve as is evident from the transition in the critical Reynolds number plot shown in Fig. 5. There is also another synchronous branch at larger wavenumbers, but the minimum of this branch occurs at a higher value of $\tilde{R}_e$.

The effect of the temporal modulation on the wavenumber of the critical disturbances is shown in Fig. 12, which plots the critical wavenumber as a function of modulation frequency, γ, for the same conditions as Fig. 5. Without modulation the critical wavenumber is 3.12. For large γ, the critical wavenumber asymptotes to this value. As γ decreases the critical wavenumber decreases slightly and then rises sharply. At each of the transitions between synchronous and subharmonic response, there is a discontinuous change in the critical wavenumber. At small γ, corresponding to large degrees of stabilization, the wavenumber behavior is complicated with no clear trend.

7. Discussion

Our numerical linear stability results are in excellent agreement with the experimental data of Walsh and Donnelly, except for low frequencies and large modulation amplitudes where the experimental results lie below the calculated critical Reynolds numbers. Both the calculations and the experiments show that modulation of the outer cylinder about zero mean stabilizes the flow when compared to the case of a stationary outer cylinder. For constant rotation of the outer cylinder, Taylor showed [1] that the critical Reynolds number is a U-shaped function of the angular velocity of the outer cylinder, and that the lowest critical Reynolds number occurs for zero outer cylinder rotation. A simple argument for the stabilization by modulation of the outer cylinder assumes that the instantaneous angular velocity of the outer cylinder can be used to characterize the instability [8]. Thus, modulation effectively moves the system into a less unstable region of the stability diagram; in fact, for sufficiently large modulations the system spends a portion of its time in the stable region of the stability diagram of the unmodulated flow. Therefore, the stabilization increases with increasing modulation amplitude. A comparison of the base flow (Fig. 1) with the temporal response of the eigenfunctions shown in Figs. 7 and 8 indicates that the quiescent interval occurs during the half-cycle when the outer cylinder velocity decreases from maximum velocity (corotation) to minimum velocity (counterrotation).

There are a number of possible explanations for the discrepancy between our calculations and the experimental results for the critical Reynolds numbers at low frequencies and large modulation amplitudes (see Fig. 5 and Table 1). Walsh and Donnelly indicate that at low frequency it becomes increasingly difficult to determine the onset of instability. In linear stability calculations, the criterion for stability is that of transient stability [18] where a disturbance may grow for part of the forcing cycle but ultimately decays. At the onset of transient instability, the eigenmodes (Figs. 7 and 8) show a quiescent interval followed by a very large amplification. Depending on the size of initial fluctuations, this large amplification might invalidate the linear theory, or alternatively might be viewed as instability in experimental observations ([18], [19]). Since disturbances are always present in experiments and since individual disturbances may grow to significant amplitude for part of the cycle, this situation may be viewed as a manifestation of secondary flow, even though an individual disturbance would decay over several cycles according to linear theory. The likelihood of this situation occurring is greater at lower frequencies, where the time period for the effect of multiple disturbances to accumulate is longer.

Finally, it is important to mention that although the present study is comprehensive, it is not exhaustive owing to the large number of parameters and the complexity exhibited by the stability boundaries. For example, it was not possible to evaluate $\tilde{R}_e$ for all wavenumbers in the entire frequency range. As shown in Fig. 11, there are multiple minimums in the plot of $\tilde{R}_e$ versus a at fixed frequency. Also, only axisymmetric disturbances were investigated here. It is possible that for certain parameter values nonaxisymmetric modes may be more unstable. It is known that for steady rotation the critical modes can be nonaxisymmetric when the cylinders rotate in opposite directions [20]. However, given the good agreement with the experimental results for all but low frequency, high amplitude modulation, it is clear that axisymmetric linear theory is still relevant for studying the effect of time-periodic forcing in the Taylor-Couette problem.

8. Acknowledgments

The first author (BTM) was supported by a National Research Council Postdoctoral Research Fellowship. The research was also supported by the Microgravity Science and Applications Program, NASA, and the Applied and Computational Mathematics Program of the Defense Advanced Research Projects Agency.

References

[1] G. I. Taylor, Phil. Trans. Roy. Soc. A **223**, 289 (1923).

[2] R. J. Donnelly, F. Reif & H. Suhl, Phys. Rev. Lett. **9**, 363 (1962).

[3] R. J. Donnelly, Proc. R. Soc. Lond. A **281**, 130 (1964).

[4] M. E. Glicksman, S. R. Coriell, & G. B. McFadden, Ann. Rev. Fluid Mech. **18**, 307 (1986).

[5] G. B. McFadden, S. R. Coriell, M. E. Glicksman & M. E. Selleck, PhysicoChemical Hydrodynamics **11**, 387 (1989).

[6] G. B. McFadden, S. R. Coriell, B. T. Murray, M. E. Glicksman & M. E. Selleck, Phys. Fluids, to appear (1990).

[7] S. Carmi & J. I. Tustaniwskyj, J. Fluid Mech. **108**, 19 (1981).

[8] T. J. Walsh & R. J. Donnelly, Phys. Rev. Lett. **60**, 700 (1988).

[9] C. F. Barenghi & C. A. Jones, J. Fluid Mech. **208**, 127 (1989).

[10] P. Hall, J. Fluid Mech. **67**, 29 (1975).

[11] G. Seminara & P. Hall, Proc. R. Soc. Lond. A **350**, 299 (1976).

[12] S. R. Coriell, M. R. Cordes, W. J. Boettinger & R. F. Sekerka, J. Crystal Growth **49**, 13 (1980).

[13] M. R. Scott & H. A. Watts, SIAM J. Numer. Anal. **14**, 40 (1977).

[14] D. Gottlieb, M. Y. Hussaini & S. A. Orszag, *Spectral Methods for Partial Differential Equations*, (SIAM-CBMS, Philadelphia, 1984).

[15] C. Canuto, M. Y. Hussaini, A. Quarteroni & T. A. Zang, *Spectral Methods in Fluid Dynamics*. (Springer-Verlag, New York, 1988).

[16] L. R. Petzold, *A Description of DASSL: A Differential/Algebraic System Solver*, SAND82-8637, Sandia National Laboratories (1982).

[17] L. R. Petzold, SIAM J. Sci. Stat. Comput., **3**, 367 (1982).

[18] S. H Davis, Ann. Rev. Fluid Mech. **8**, 57 (1976).

[19] R. G. Finucane & R. E. Kelly, Int. J. Heat Mass Transfer **19**, 71 (1976).

[20] E. R. Krueger, A. Gross & R. C. DiPrima, J. Fluid Mech. **24**, 521 (1966).

Table I. Comparison of $\tilde{R}_c$ from the experimental data of Walsh and Donnelly and the present calculations for various modulation amplitudes, ϵ, at fixed frequency, $\gamma = 2.3$, with $\eta = 0.88$. The calculated wavenumber, a, and mode type are also shown.

ϵ	0.0	0.3	0.5	0.7	0.9	1.5	2.0
$\tilde{R}_c$ (Data)	44.5	45.9	47.8	50.8	55.5	73.3	86.4
$\tilde{R}_c$ (Calc)	44.5	45.4	47.2	50.5	56.6	83.9	97.2
a (Calc)	3.1	3.1	3.1	3.1	3.2	4.3	4.5
Mode	–	syn	syn	syn	syn	syn	sub

Figure Captions

Figure 1. Azimuthal base flow velocity, $v^{(0)}$ as a function of the radial coordinate, r, for various fractional times through half a period for $\gamma = 2$, $\eta = 0.88$, and $\epsilon = 1.5$.

Figure 2. Azimuthal base flow velocity, $v^{(0)}$ as a function of the radial coordinate, r, for various fractional times through half a period for $\gamma = 6$, $\eta = 0.88$, and $\epsilon = 1.5$.

Figure 3. Critical values of $\tilde{R}_e$ as a function of γ for $\eta = 0.719$ and $\epsilon = 1.5$. The points are the experimental results of Walsh and Donnelly; the curves are the present linear theory (solid curve - synchronous response, dotted curve - subharmonic response).

Figure 4. Critical values of $\tilde{R}_e$ as a function of γ for $\eta = 0.88$ and $\epsilon = 0.5$. The points are the experimental results of Walsh and Donnelly; the solid curve is the present linear theory.

Figure 5. Critical values of $\tilde{R}_e$ as a function of γ for $\eta = 0.88$ and $\epsilon = 1.5$. The points are the experimental results of Walsh and Donnelly; the curves are the present linear theory (solid curve - synchronous response, dotted curve - subharmonic response).

Figure 6. Linear eigenfunction velocity components $\hat{u}(r,t)$ and $\hat{v}(r,t)$ plotted for one forcing period over the spatial domain for $\gamma = 6$, $\eta = 0.88$, and $\epsilon = 1.5$ (synchronous response).

Figure 7. Linear eigenfunction velocity components $\hat{u}(r,t)$ and $\hat{v}(r,t)$ plotted for one forcing period (starting at $t = 0.25$) over the spatial domain for $\gamma = 2$, $\eta = 0.88$, and $\epsilon = 1.5$ (synchronous response).

Figure 8. Linear eigenfunction velocity components $\hat{u}(r,t)$ and $\hat{v}(r,t)$ plotted for two forcing periods (starting at $t = 0.50$) over the spatial domain for $\gamma = 2$, $\eta = 0.88$, and $\epsilon = 1.5$ (subharmonic response).

Figure 9. The m*th* temporal Fourier coefficient of the v velocity component at a fixed spatial point as a function of m for the linear eigenfunctions shown in Fig. 6 (solid curve) and Fig. 7 (dotted curve).

Figure 10. The n*th* Chebyshev spectral coefficient of the v velocity component at a fixed time as a function of n for the linear eigenfunctions shown in Fig. 6 (solid curve) and Fig. 8 (dotted curve).

Figure 11. Values of $\tilde{R}_c$ as a function of wavenumber, a, for $\gamma = 2.0$, $\eta = 0.88$ and $\epsilon = 1.5$. (solid curve - synchronous response, dotted curve - subharmonic response).

Figure 12. Critical values of a as a function of γ for the same parameters as Fig. 5. (solid curve - synchronous response, dotted curve - subharmonic response).

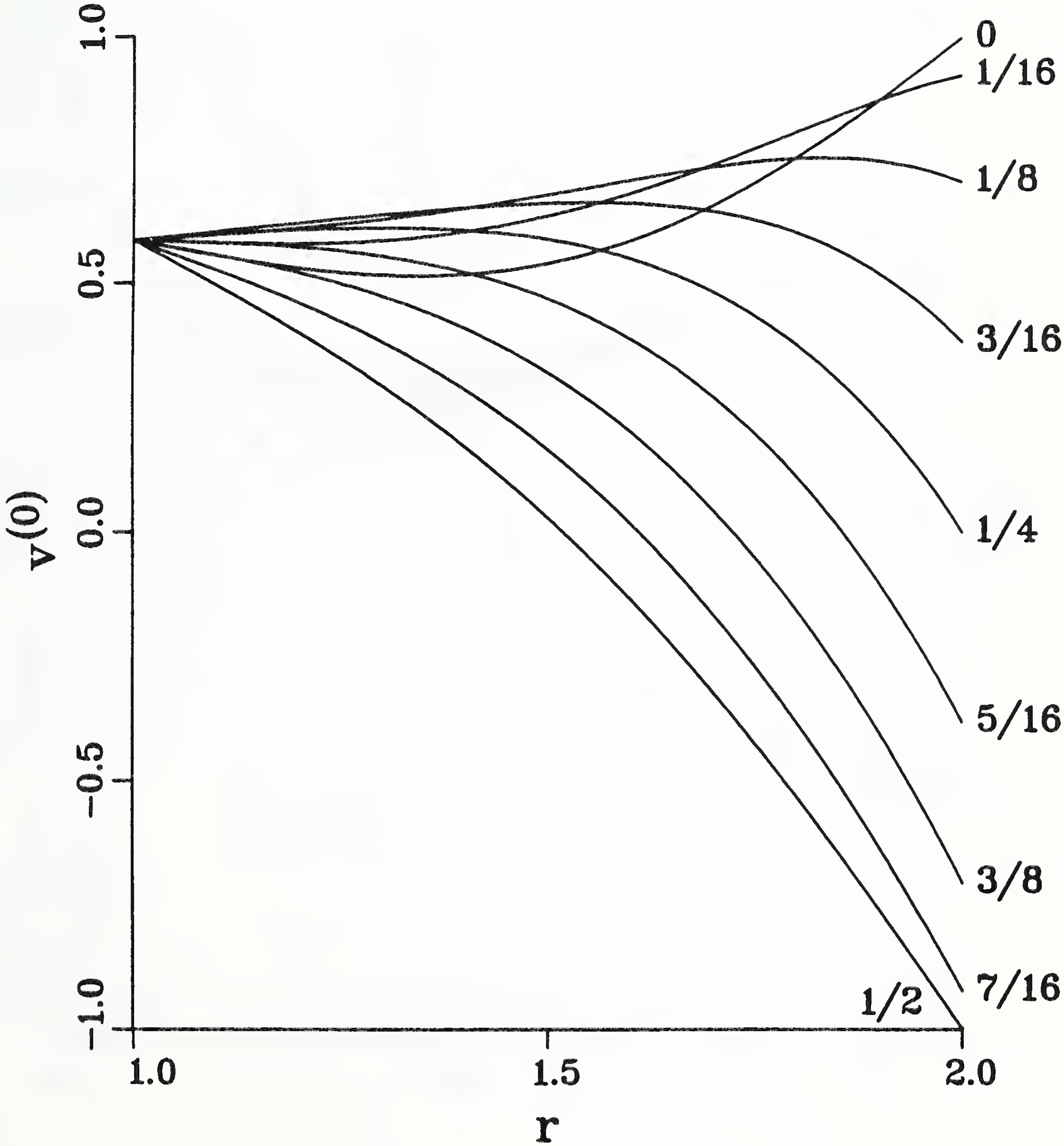

Figure 1

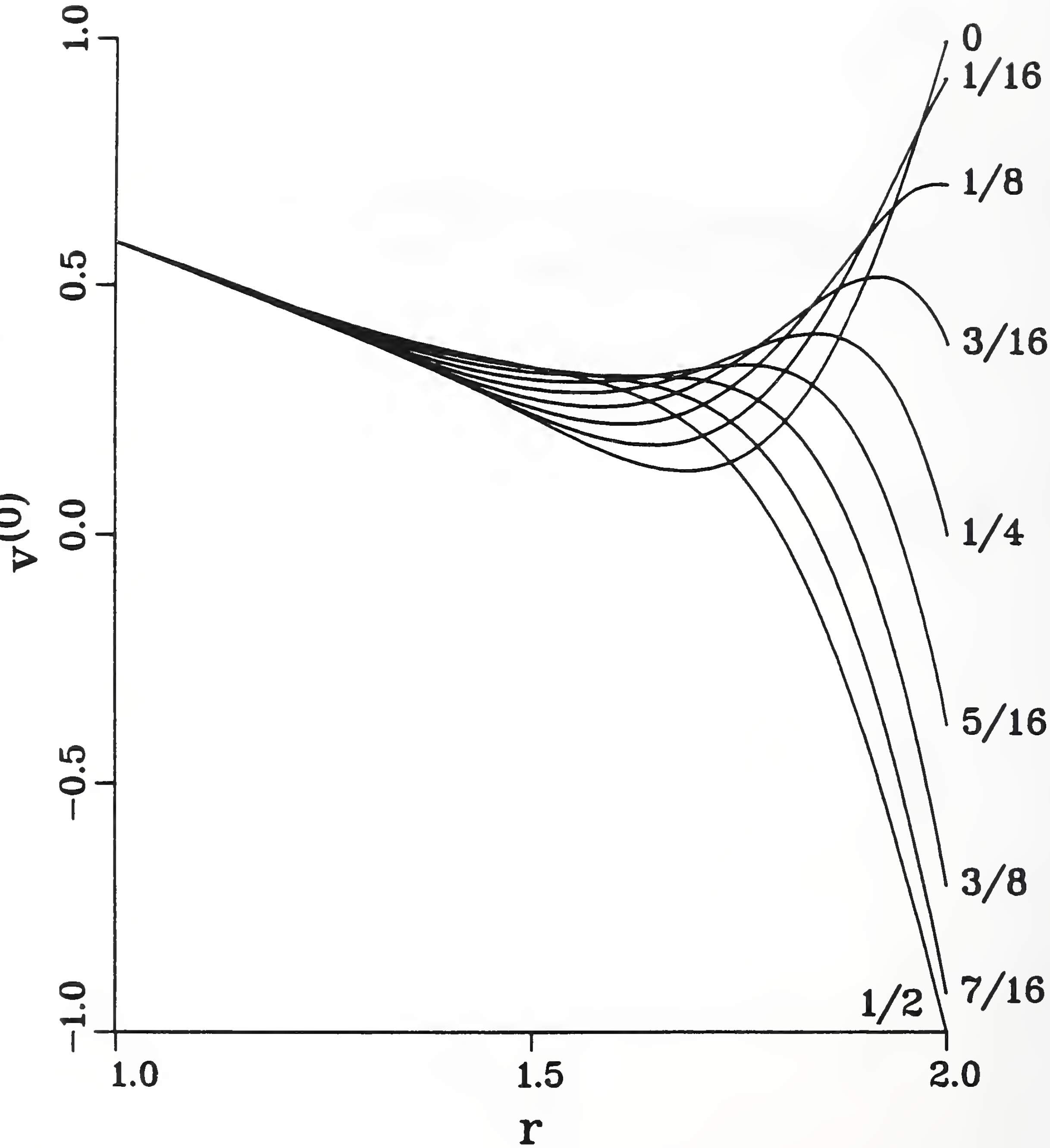

Figure 2

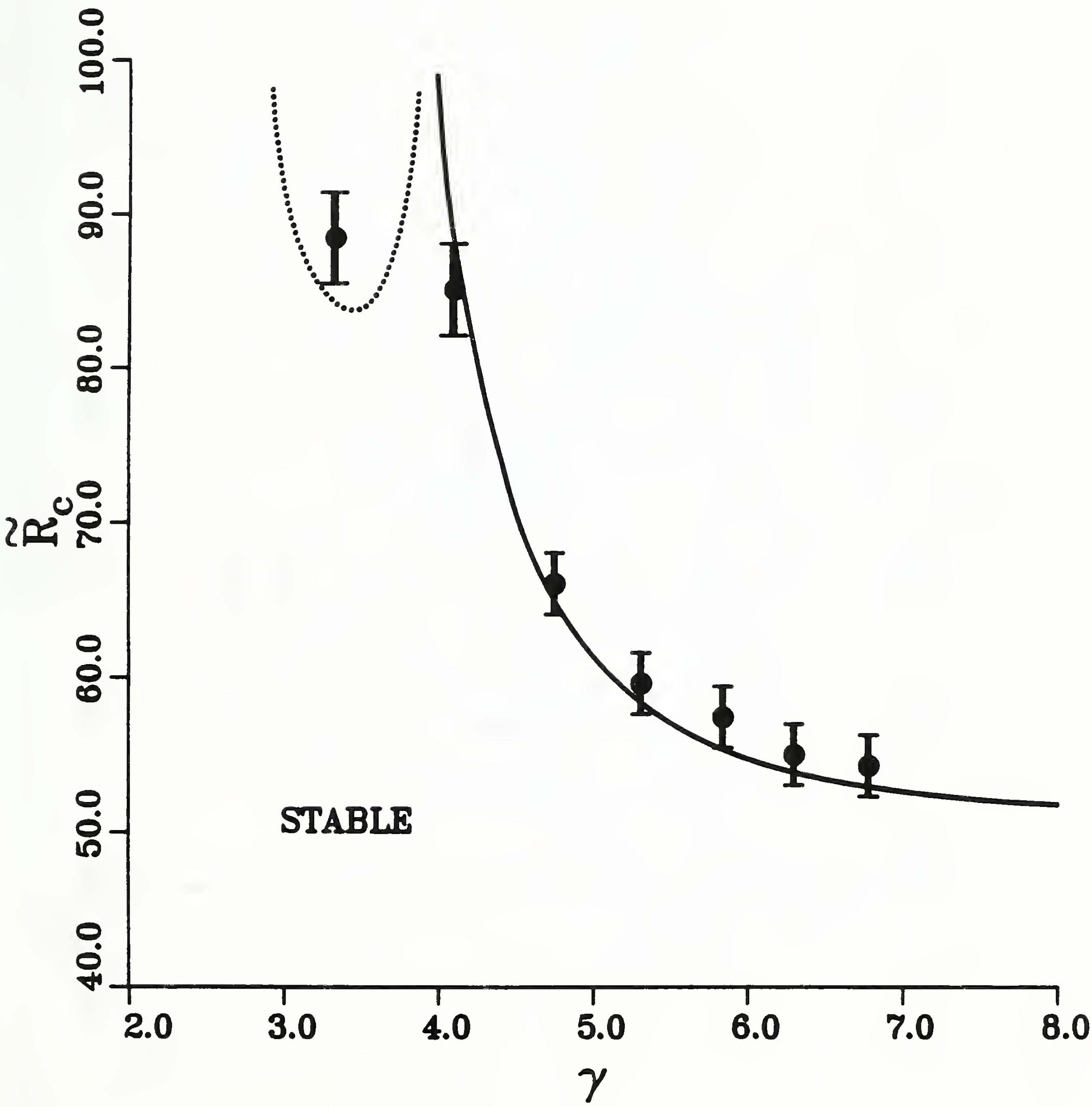

100.0
90.0
80.0
70.0
60.0
50.0
40.0
$\tilde{R}_c$
STABLE
2.0
3.0
4.0
5.0
6.0
7.0
8.0
γ

Figure 3

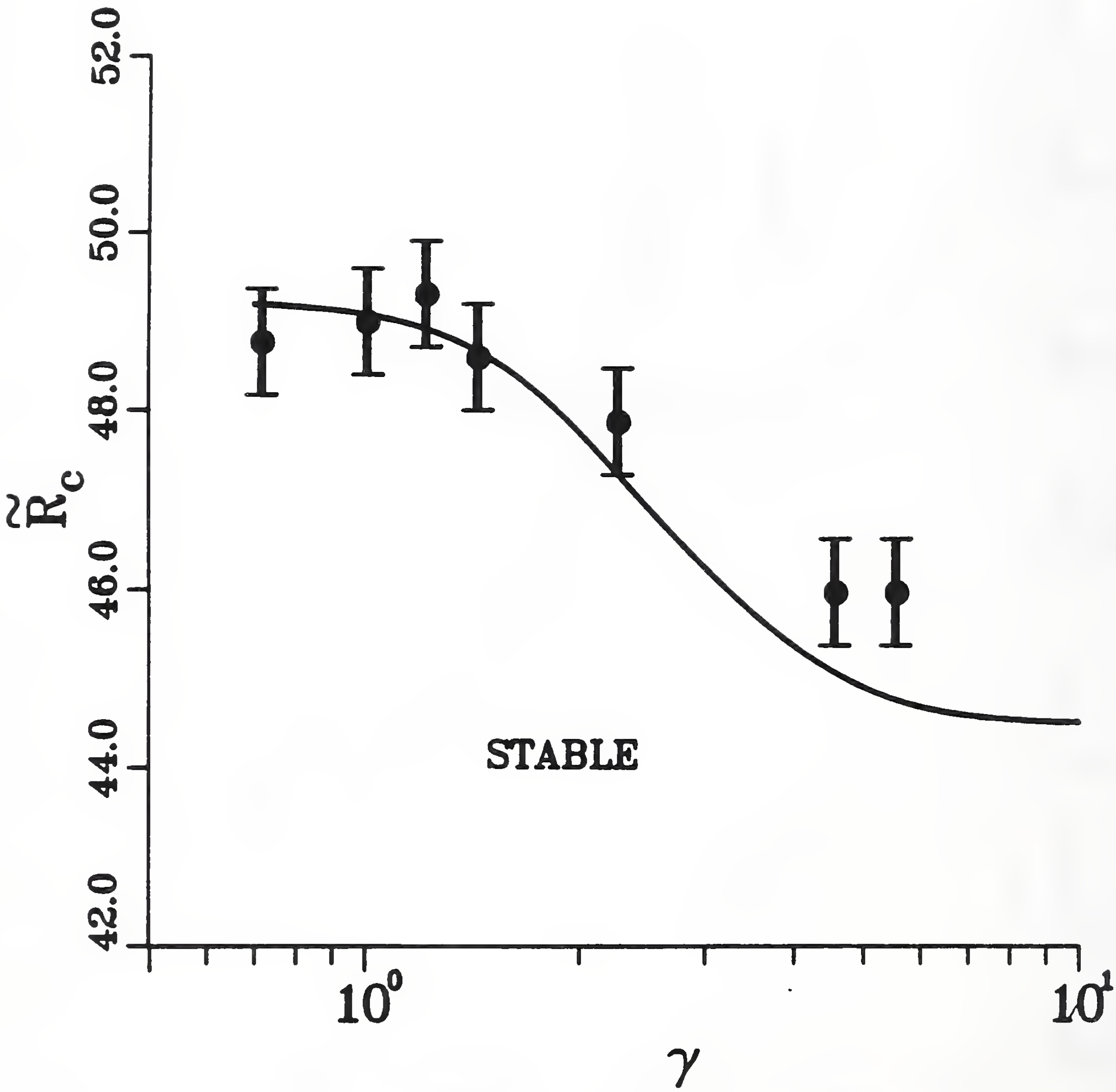

Figure 4

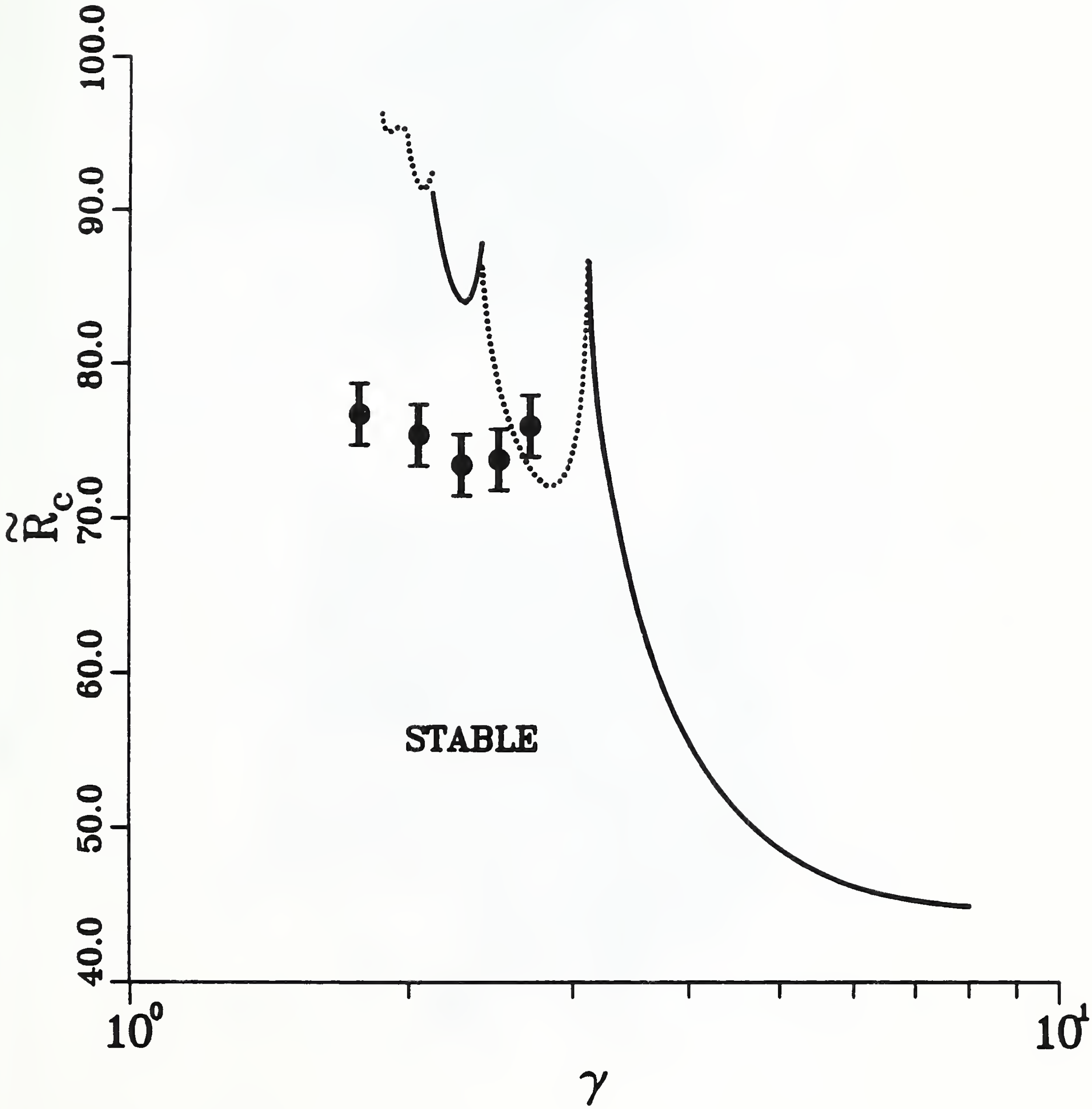

Figure 5

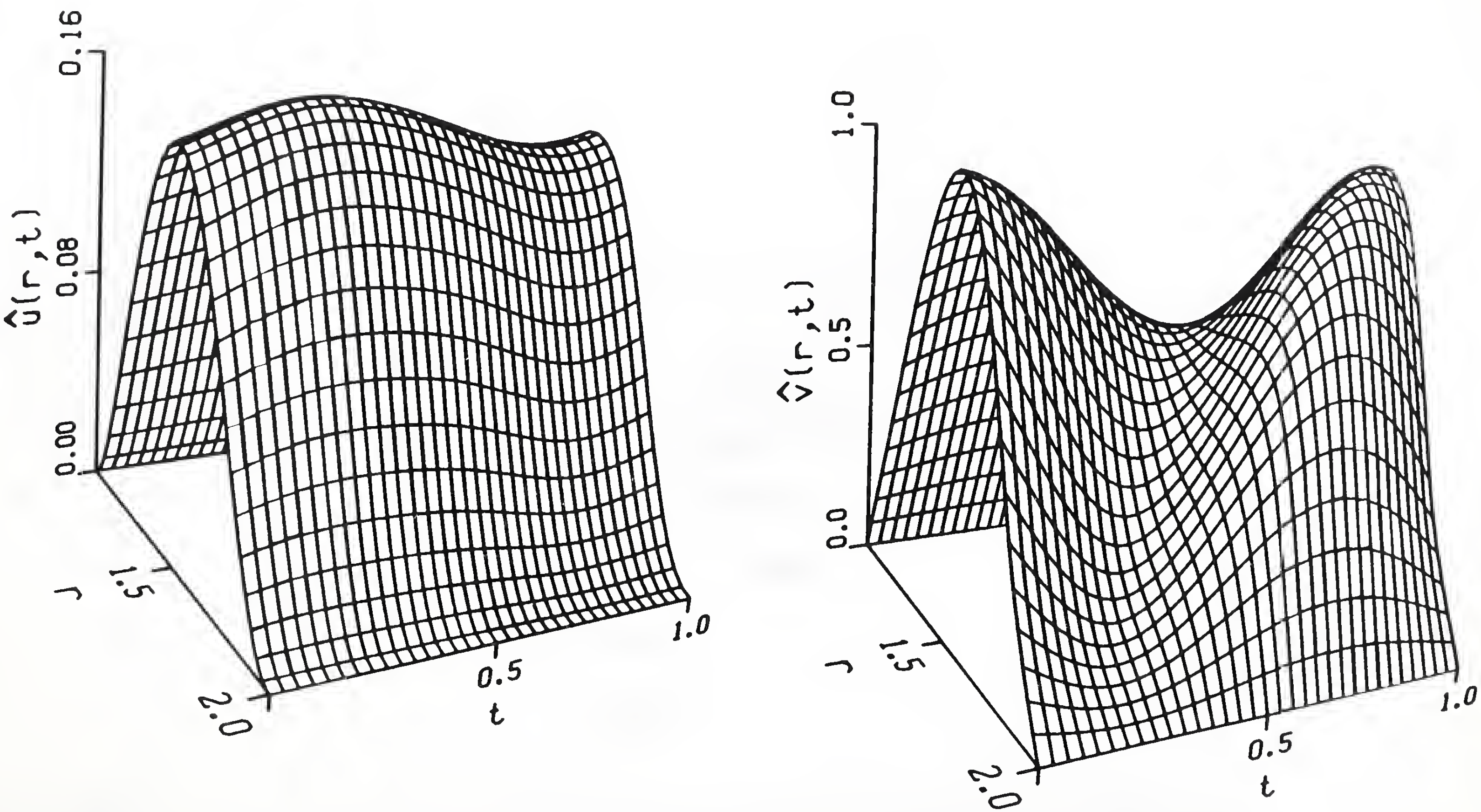

Figure 6

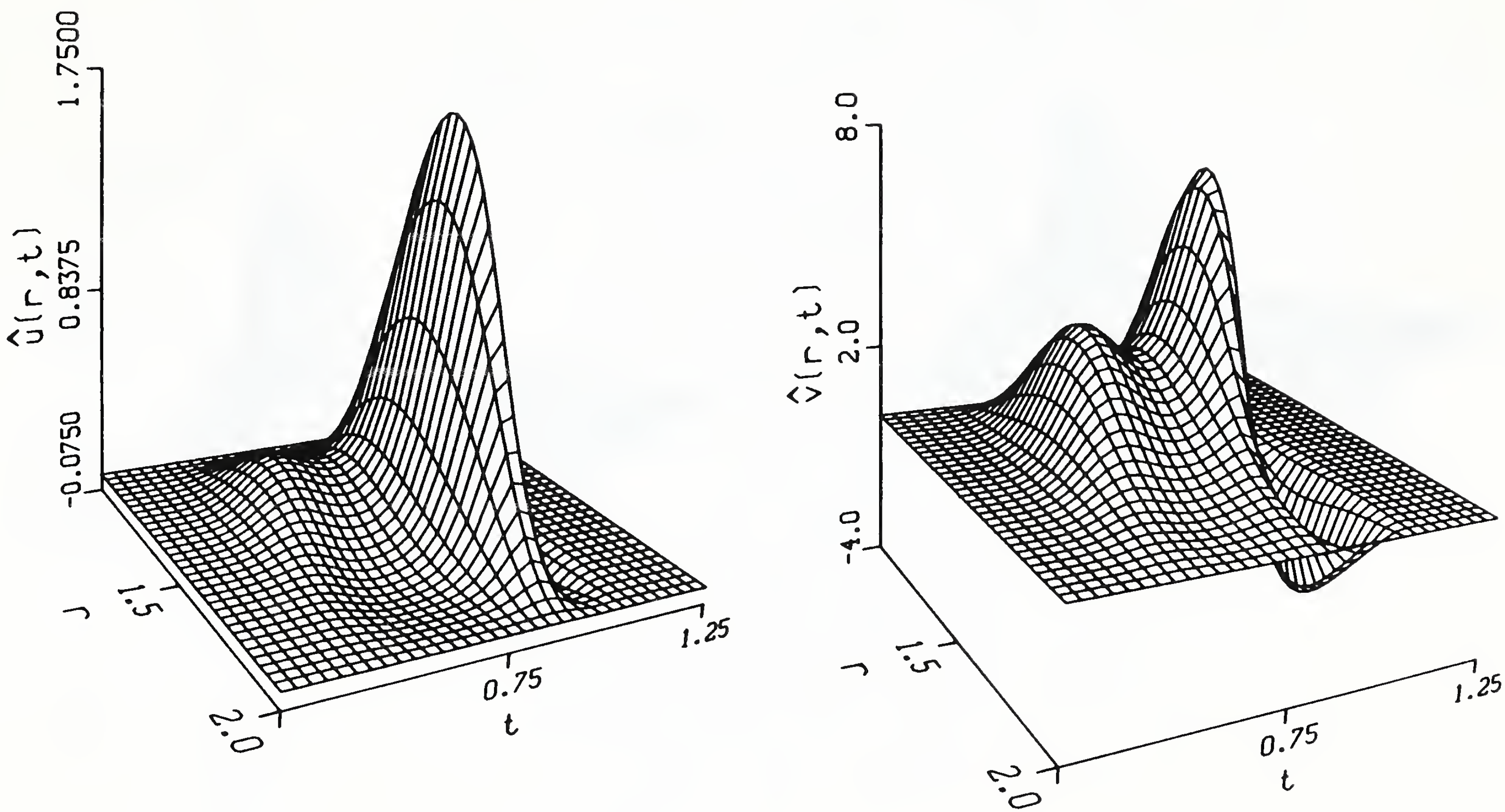

û(r,t)
1.7500
0.8375
-0.0750
r
1.5
2.0
t
0.75
1.25
v̂(r,t)
8.0
2.0
-4.0
r
1.5
2.0
t
0.75
1.25

Figure 7

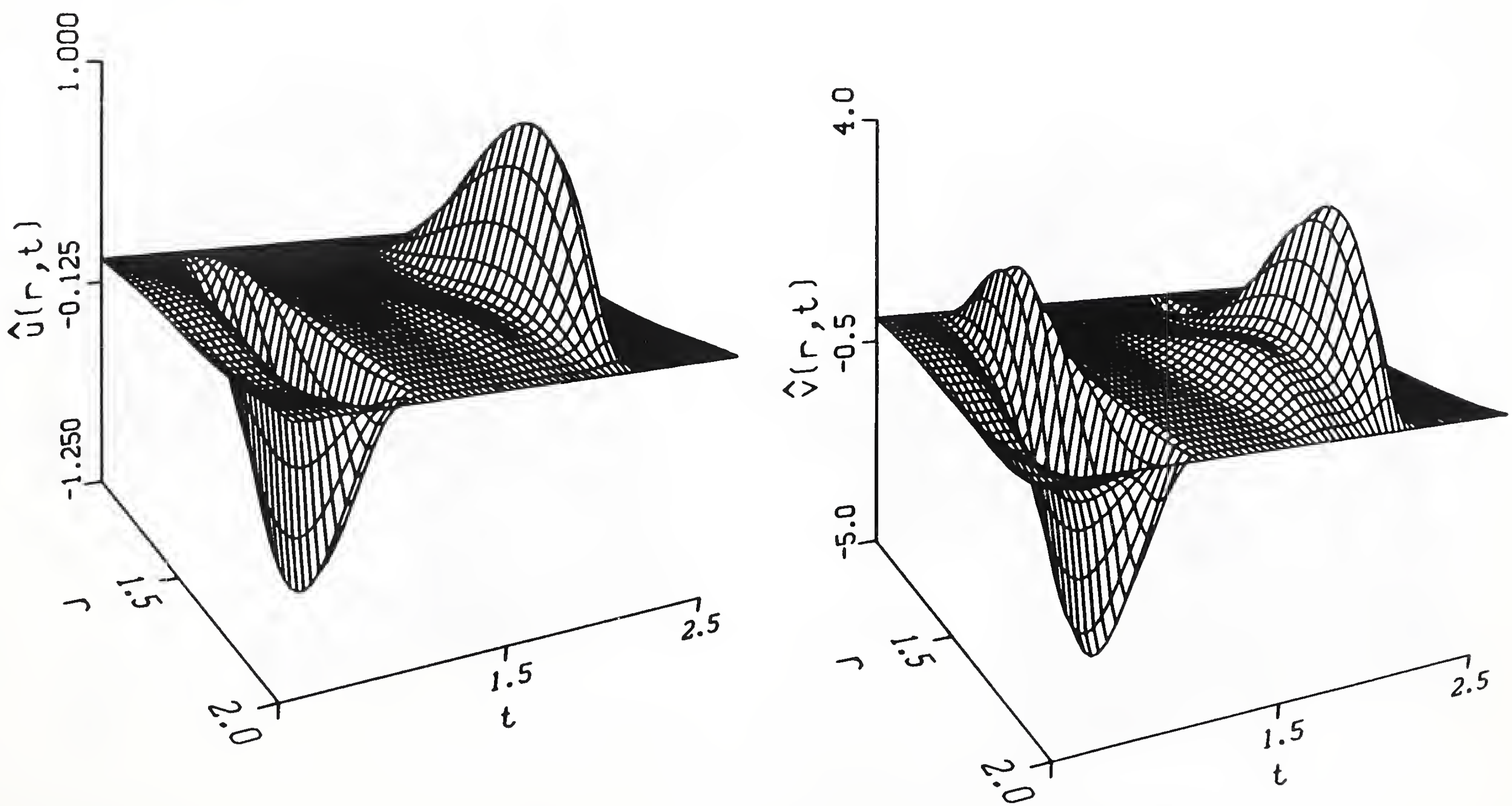
1.000
-0.125
-1.250
$\hat{u}(r,t)$
r
1.5
2.0
1.5
2.5
t
4.0
-0.5
-5.0
$\hat{v}(r,t)$
r
1.5
2.0
1.5
2.5
t

Figure 8

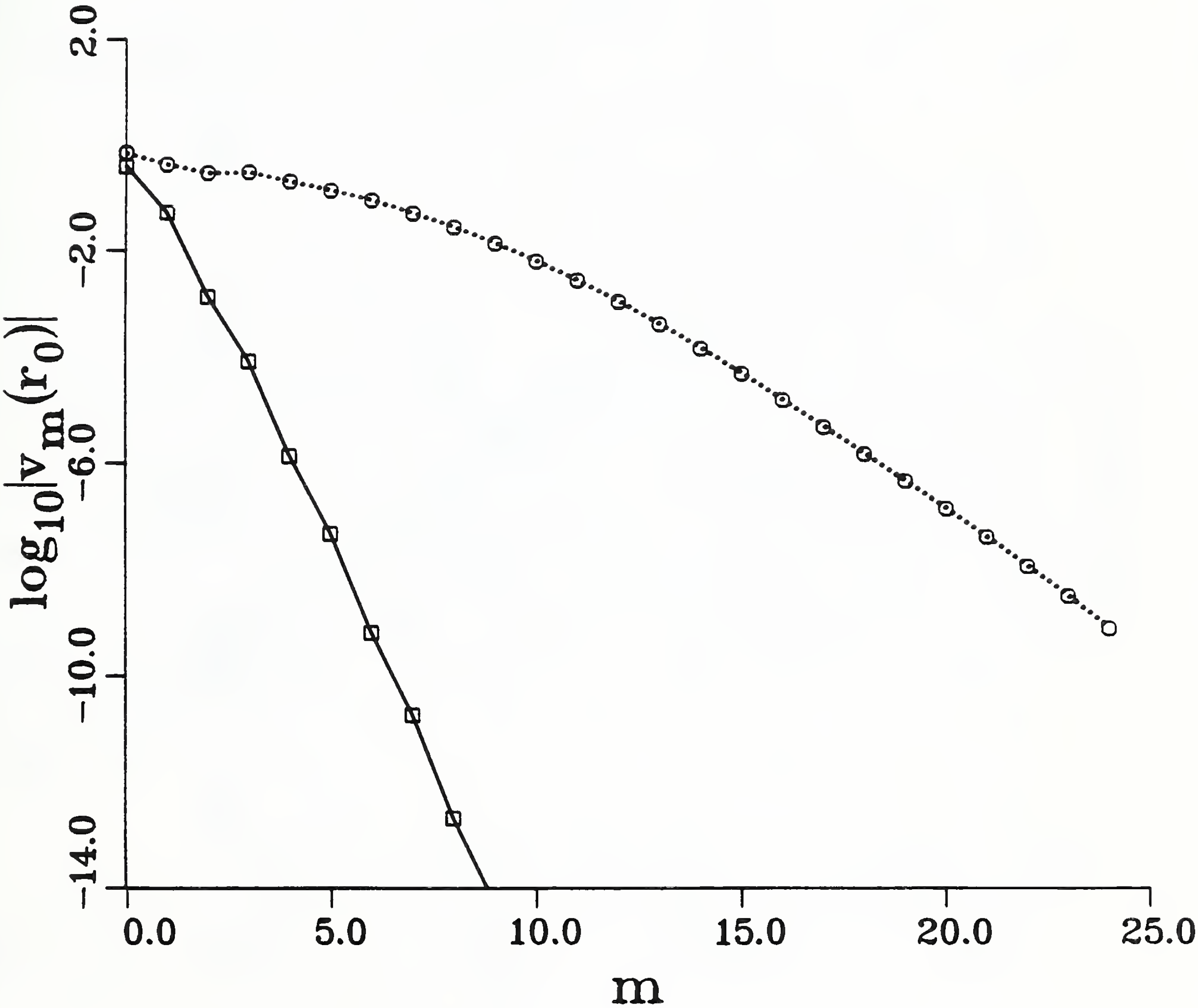

Figure 9

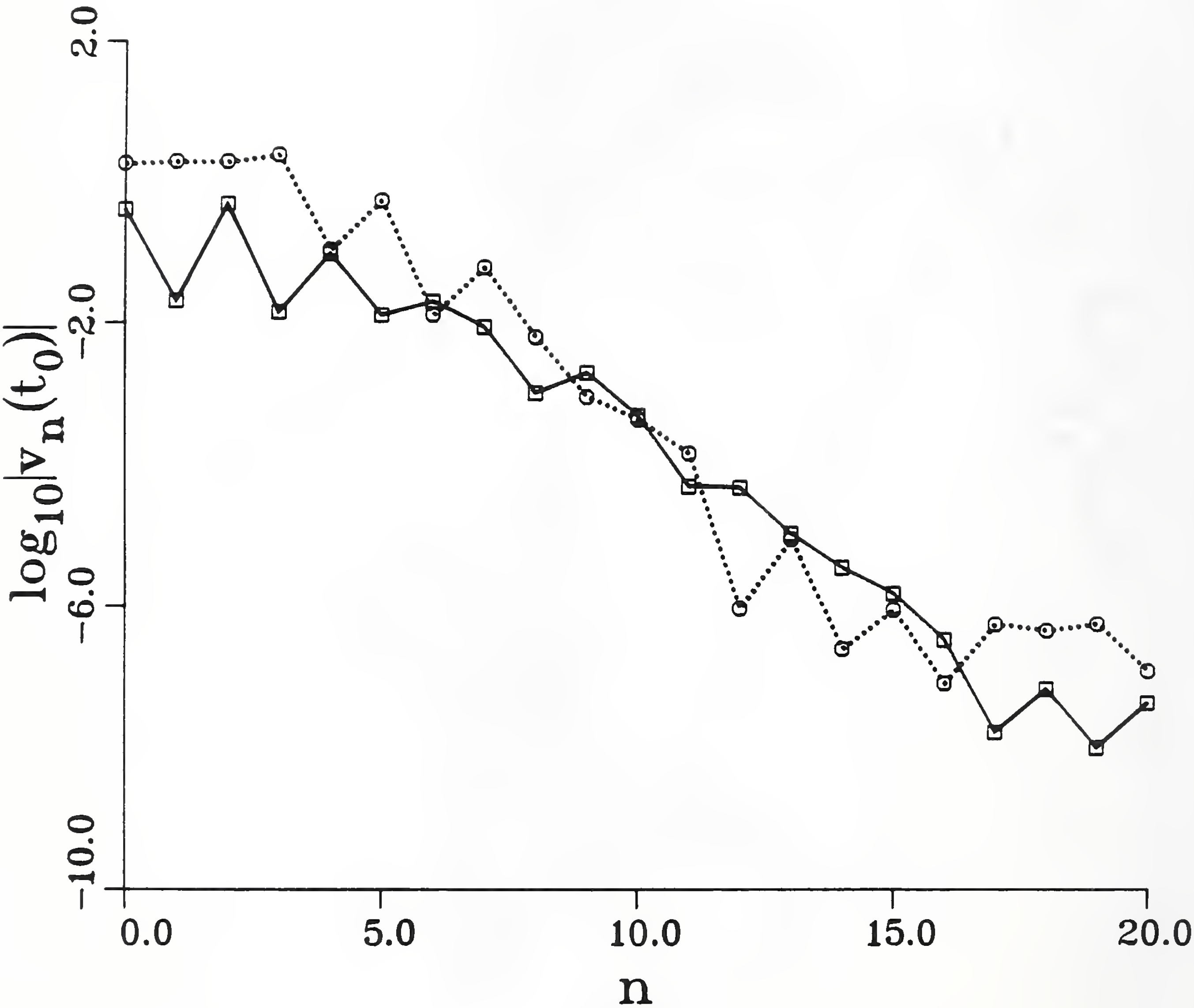

Figure 10

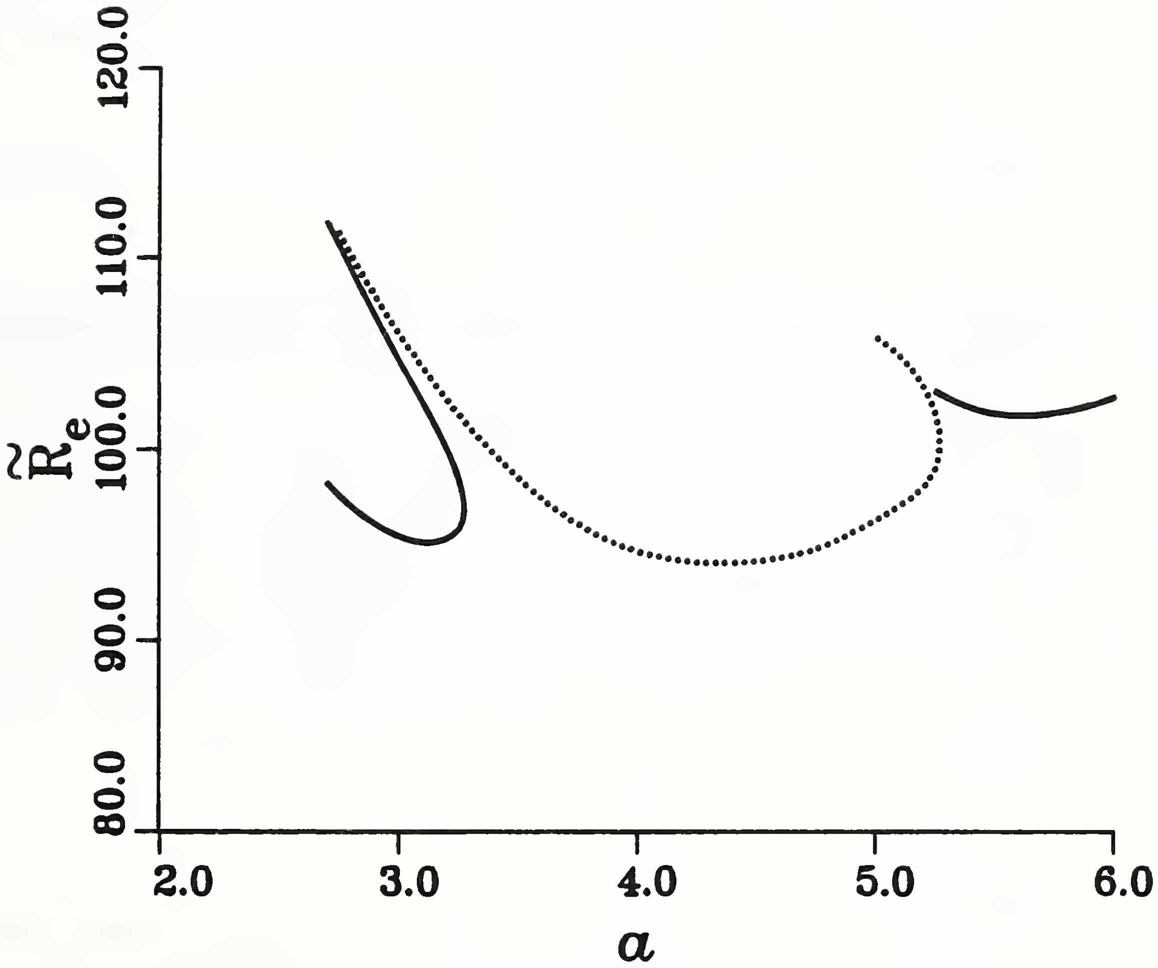

Figure 11

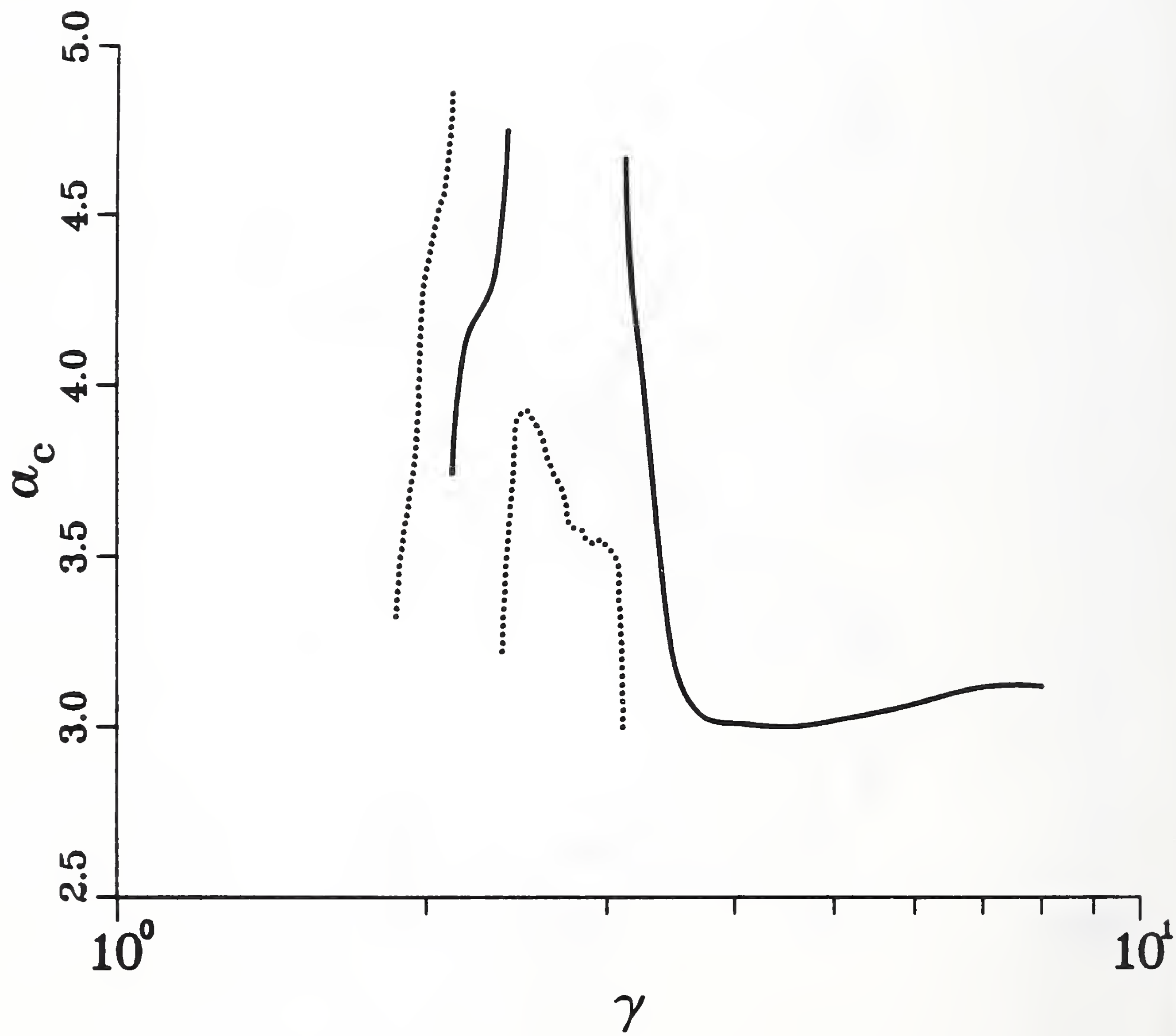

Figure 12

NIST-114A (REV. 3-89)

U.S. DEPARTMENT OF COMMERCE
NATIONAL INSTITUTE OF STANDARDS AND TECHNOLOGY

BIBLIOGRAPHIC DATA SHEET

1. PUBLICATION OR REPORT NUMBER
NISTIR 90-4283

2. PERFORMING ORGANIZATION REPORT NUMBER

3. PUBLICATION DATE
APRIL 1990

4. TITLE AND SUBTITLE

Stabilization of Taylor-Couette Flow due to Time-Periodic Outer Cylinder Oscillation

5. AUTHOR(S)

B. T. Murray, G. B. McFadden, and S. R. Coriell

6. PERFORMING ORGANIZATION (IF JOINT OR OTHER THAN NIST, SEE INSTRUCTIONS)

U.S. DEPARTMENT OF COMMERCE
NATIONAL INSTITUTE OF STANDARDS AND TECHNOLOGY
GAITHERSBURG, MD 20899

7. CONTRACT/GRANT NUMBER

8. TYPE OF REPORT AND PERIOD COVERED

9. SPONSORING ORGANIZATION NAME AND COMPLETE ADDRESS (STREET, CITY, STATE, ZIP)

10. SUPPLEMENTARY NOTES

☐ DOCUMENT DESCRIBES A COMPUTER PROGRAM; SF-185, FIPS SOFTWARE SUMMARY, IS ATTACHED.

11. ABSTRACT (A 200-WORD OR LESS FACTUAL SUMMARY OF MOST SIGNIFICANT INFORMATION. IF DOCUMENT INCLUDES A SIGNIFICANT BIBLIOGRAPHY OR LITERATURE SURVEY, MENTION IT HERE.)

The linear stability of circular Couette flow between concentric infinite cylinders is considered for the case when the inner cylinder is rotated at a constant angular velocity and the outer cylinder is driven sinusoidally in time with zero mean rotation. This configuration was studied experimentally by Walsh and Donnelly. The critical Reynolds numbers calculated from linear stability theory agree well with the experimental values, except at large modulation amplitudes and small frequencies. The theoretical values are obtained using Floquet theory implemented in two distinct approaches: 1) a truncated Fourier series representation in time and 2) a fundamental solution matrix based on a Chebyshev-pseudospectral representation in space. For large amplitude, low frequency modulation, the linear eigenfunctions are temporally complex consisting of a quiescent region followed by rapid change in the perturbed flow velocities.

12. KEY WORDS (6 TO 12 ENTRIES; ALPHABETICAL ORDER; CAPITALIZE ONLY PROPER NAMES; AND SEPARATE KEY WORDS BY SEMICOLONS)

Floquet Theory; Fourier spectral method; hydrodynamic stability; pseudospectral collocation; Taylor-Couette flow; time-periodic modulation

13. AVAILABILITY

X	UNLIMITED
	FOR OFFICIAL DISTRIBUTION. DO NOT RELEASE TO NATIONAL TECHNICAL INFORMATION SERVICE (NTIS).
	ORDER FROM SUPERINTENDENT OF DOCUMENTS, U.S. GOVERNMENT PRINTING OFFICE, WASHINGTON, DC 20402.
X	ORDER FROM NATIONAL TECHNICAL INFORMATION SERVICE (NTIS), SPRINGFIELD, VA 22161.

14. NUMBER OF PRINTED PAGES
35

15. PRICE
A03

ELECTRONIC FORM